

Oxygen isotope heterogeneities in the earliest protosolar gas recorded in a meteoritic calcium–aluminum-rich inclusion

Jérôme Aléon^{a,b,*}, Ahmed El Goresy^c, Ernst Zinner^d

^a Centre de Recherches Petrographiques et Géochimiques, 15 rue Notre-Dame des Pauvres, BP 20, 54501 Vandoeuvre-lès-Nancy, France

^b Centre de Spectrométrie Nucléaire et de Spectrométrie de Masse, Bat. 104, 91405 Orsay Campus, France

^c Bayerisches Geoinstitut, Universität Bayreuth, D-95440 Bayreuth, Germany

^d Laboratory for Space Sciences and the Physics Department, Campus Box 1105, Washington University, One Brookings Drive, Saint Louis MO 63130, USA

Received 27 February 2007; received in revised form 30 August 2007; accepted 4 September 2007

Available online 12 September 2007

Editor: R.W. Carlson

Abstract

Combined petrologic, oxygen and magnesium isotopic and trace element analyses of a compound calcium–aluminum-rich inclusion (CAI) from the Efremovka reduced CV3 carbonaceous chondrite reveal that it consists of a Mg-rich, ¹⁶O-rich xenolithic CAI, previously altered in the nebula, that impacted an extensively molten, ¹⁶O-depleted, type A host CAI shortly before the end of the host's crystallization. Convolved regions in the xenolith were probably formed by rapid crystallization of the partial melt produced during impact.

Oxygen isotopic ratios in the host CAI are correlated both with melilite chemistry and location in the inclusion. The region immediately inside the Wark–Lovering rim of the CAI consists of ¹⁶O-rich gehlenite with $\Delta^{17}\text{O}$ ranging down to -20% but melilite becomes progressively ¹⁶O-poor ($\Delta^{17}\text{O} \sim 0\%$) and Mg-rich towards the interior. In the absence of Mg isotopic fractionation, this variation is best attributed to O isotopic exchange between the nebular gas and the partially molten inclusion during its crystallization. This event lasted less than 200 h, which implies that the host CAI was transported between two nebular reservoirs with distinct O isotopic compositions during this time. Examination of possible transport mechanisms suggests that the transport occurred over a distance of less than 1 astronomical unit. The close-to-canonical ²⁶Al/²⁷Al ratio of 4.1×10^{-5} determined from both inclusions implies that at most 670,000 yr after the birth of the Solar System, the ¹⁶O-rich reservoir was spatially limited and an ¹⁶O-poor reservoir with typical planetary isotopic composition was available for planet formation.

© 2007 Elsevier B.V. All rights reserved.

Keywords: protosolar nebula; oxygen isotopes; refractory inclusions; meteorites; magnesium isotopes

1. Introduction

Oxygen isotopic compositions in Solar System materials define a mixing trend between an ¹⁶O-rich component, which is preserved in calcium–aluminum-rich inclusions (CAIs) from chondritic meteorites, and a dominant ¹⁶O-poor component commonly observed in planetary materials (Clayton et al., 1973, 1977). While

* Corresponding author. Centre de Spectrométrie Nucléaire et de Spectrométrie de Masse, Bat. 104, 91405 Orsay Campus, France.

E-mail addresses: Jerome.Aleon@csnsm.in2p3.fr (J. Aléon), ahmed.elgoresy@uni-bayreuth.de (A. El Goresy), ekz@wustl.edu (E. Zinner).

CAIs, the oldest objects of the Solar System (e.g., Amelin et al., 2002), and rare chondrules (Kobayashi et al., 2003; Jones et al., 2004) show 5% ^{16}O excesses relative to the Earth oceans, the oxygen isotopic compositions of most planetary materials (including the bulk Earth, the Moon, Martian meteorites, and bulk asteroidal meteorites) cluster within $\sim 1\%$ (Clayton, 1993, 2004). The recent discovery of ^{16}O -excesses in solar wind (Hashizume and Chaussidon, 2005) implanted in lunar soils supports proposals that the whole protosolar nebula was initially ^{16}O -rich and became ^{16}O -poor by isotope-selective photodissociation of CO before the end of planetary accretion (Clayton, 2002; Yurimoto and Kuramoto, 2004; Lyons and Young, 2005), so that most planetary materials are ^{16}O -poor while the Sun is still ^{16}O -rich. This view has recently been challenged (Ireland et al., 2006) though not confirmed (Ireland et al., 2007) and the mechanism responsible for oxygen isotopic variations in the protosolar nebula (PSN) is still debated: although a nucleosynthetic origin for the ^{16}O excess (Clayton et al., 1973, 1977) is now discarded, mass-independent isotopic fractionation is commonly advocated (Thiemens and Heidenreich, 1983; Robert, 2004; Marcus, 2004; Nuth et al., 2006). It is thus essential to unravel the timing of the evolution of O isotopic reservoirs in the PSN to determine which model is correct. Previous studies based on time differences between the formation of CAIs and of chondrules (Krot et al., 2005a,b) have shown that the evolution from a ^{16}O -rich PSN to a ^{16}O -poor PSN took place in less than a million years.

Coarse-grained igneous CAIs from CV3 carbonaceous chondrites are thought to be condensates from the PSN that later experienced complex igneous histories (Grossman, 1972; MacPherson, 2004). Most of these CAIs consist of minerals with both ^{16}O -rich and ^{16}O -poor isotopic compositions (Clayton et al., 1977; Clayton, 1993; McKeegan and Leshin, 2001). Spinel and Al-(Ti)-rich clinopyroxene are usually ^{16}O -rich, whereas anorthite and melilite are commonly ^{16}O -poor. The ^{16}O -rich composition was attributed to the preservation of the initial PSN composition acquired by direct condensation from the gas (Krot et al., 2002) or to the preservation of the composition of a local ^{16}O -rich gas produced by evaporation of ^{16}O -rich dust (Scott and Krot, 2001; Itoh and Yurimoto, 2003). However, the origin of the ^{16}O -poor component is still unclear. Although numerous mechanisms how CAIs recorded the O isotope evolution of the solar gas have been investigated (Clayton et al., 1977; Ryerson and McKeegan, 1994; Yurimoto et al., 1994; Yurimoto et al., 1998; Wasson et al., 2001), none was able to account for all observations. To gain information on the oxygen isotope variations in the PSN, it is thus essential to

understand the events that are associated with the change in oxygen isotopic composition of CAI minerals.

A unique CAI from the reduced CV3 chondrite Efremovka (El Goresy and Zinner, 1994) offered us the opportunity to decipher the O isotopic compositional dichotomy of coarse-grained CAIs in CV3 chondrites and unravel the evolution of the oxygen isotopic composition in the early Solar System. Efremovka inclusion E49 is a compound CAI, a rare type of CAIs made of several lithologic units that were once individual CAIs, free-floating in the PSN. Previous oxygen isotopic studies of compound CAIs have shown that the relationship between the different lithological units is potentially useful for understanding how CAIs record the oxygen isotopic composition of the nebular gas (Kim et al., 2002; Aléon et al., 2005). Magnesium isotopes and trace elements in this inclusion have previously been reported (El Goresy and Zinner, 1994); they provide complementary chronometric and petrologic tracers to its formation.

2. Analytical methods

Oxygen isotopes were measured in two sessions with the Cameca IMS 1270 ion microprobe at CRPG in Nancy, France. Isotopic ratios are reported as permil deviations from those of Standard Mean Ocean Water ($\delta^X\text{O} = [{}^X\text{O}/{}^{16}\text{O}_{\text{sample}} - {}^X\text{O}/{}^{16}\text{O}_{\text{SMOW}}] / [{}^X\text{O}/{}^{16}\text{O}_{\text{SMOW}}] \times 1000$) where $X=17$ or 18. ^{16}O excesses are reported as ^{17}O deviations from the terrestrial mass fractionation line ($\Delta^{17}\text{O} = \Delta^{17}\text{O} - 0.52 \times \Delta^{18}\text{O}$). An unusually large spread of ratios measured in standards was observed during multi-collection analyses with simultaneous detection of the three oxygen isotopes. To limit potential problems associated with the multi-collection detectors, the second profile and duplicates were measured in mono-collection mode by magnetic peak jumping from mass to mass. The spread of the multi-collection data and the larger analytical errors for the mono-collection data resulted in uncertainties for the instrumental mass fractionation that were propagated to the CAI data and preclude a detailed analysis of small mass fractionation effects in E49. Still, the overall uncertainty in $\Delta^{17}\text{O}$ measured in standards is smaller than 1.4‰ (2σ) for multi-collection analyses and 1.0‰ (2σ) for mono-collection analyses. All reported errors are 2σ standard error of the mean and include analytical errors and uncertainties in the instrumental mass fractionation.

Magnesium isotopes and Rare Earth Element (REE) patterns were measured with the Cameca IMS 3F ion microprobe at Washington University, Saint Louis, USA. Chemical compositions of melilite and other constituents in xenolith and host were determined with a fully automated

computer controlled ARL-SEMQ electron microprobe at the Max-Planck-Institut für Kernphysik, Heidelberg, Germany, with the Cameca SX 100 electron microprobes at the Service Commun de Microanalyse, University Henri Poincaré, Nancy, France, and at the CAMPARIS analytical facility, University Paris VI, Paris, France.

3. Results

3.1. Mineralogy and petrology

3.1.1. Host

E49 is a compact type A CAI dominated by melilite with Mg concentrations ranging from Åk_1 to Åk_{40} (proportions of Åkermanite , the Mg-rich melilite end-

member) and is surrounded by a Wark–Lovering rim (Wark and Lovering, 1977) (Fig. 1). While melilite in the core of the inclusion is more Åkermanitic ($\sim \text{Åk}_{20}$ – Åk_{40}), it becomes progressively gehlenitic towards the rim (down to Åk_1). The host contains minor isolated spinel, perovskite, Al–Ti-rich clinopyroxene and FeNi metal grains distributed in melilite. The Wark–Lovering rim consists of spinel, melilite and pyroxene monomineralic layers starting from the inside of the rim. Perovskite is abundant in the host melilite at the contact with the spinel layer. The rim is faulted and repeated in several locations. An iron–oxide-filled crack of probable terrestrial origin occurs along $\sim 25\%$ of the rim and accounts for detectable amounts of FeO in melilite along the contact with the crack (0.15–0.41 wt%) (Fig. 1).

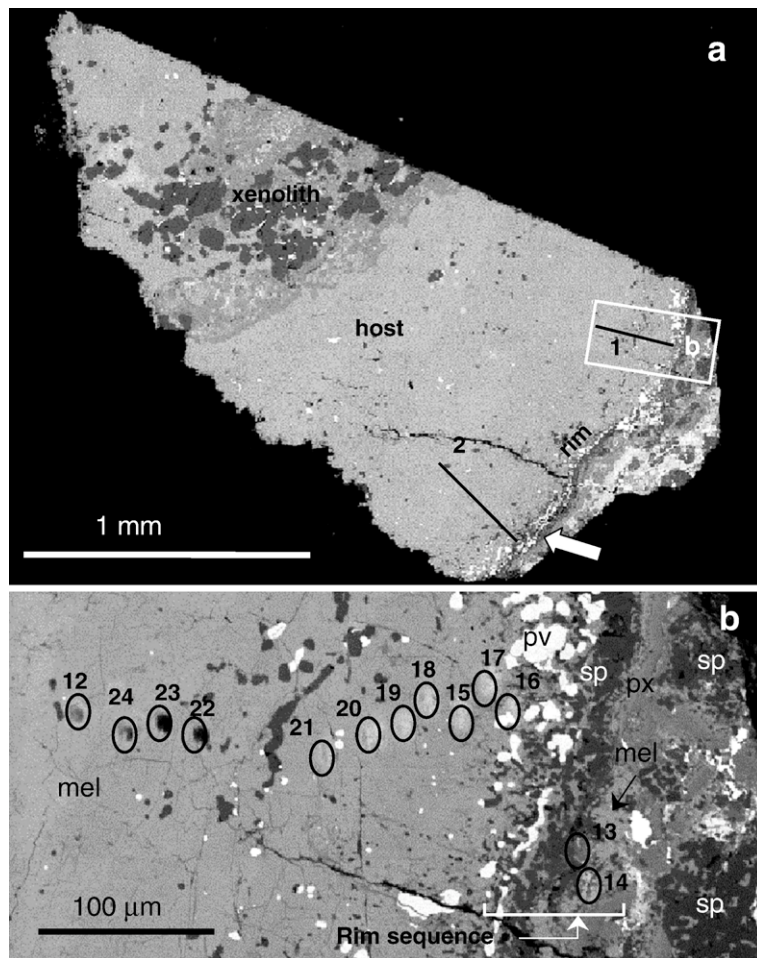


Fig. 1. Backscattered electron (BSE) micrographs of E49. a. General view of the inclusion. The xenolith and the host inclusion are indicated, as well as the Wark–Lovering rim. Lines 1 and 2 indicate the path of the oxygen isotope profiles. The white arrow points to the iron–oxide-filled crack. The rectangle indicates the location of Fig. 1b. b. Detailed BSE micrograph of area around oxygen isotope profile 1. Ion probe pits are indicated with ellipses and numbered according to Table 2. Spot 16 overlaps melilite and perovskite, spots 13 is dominantly on spinel from the rim and spot 14 is dominantly on melilite from the rim; all other spots are on 100% melilite from the host CAI. Abbreviations: sp — spinel; px — pyroxene; mel — melilite; pv — perovskite.

3.1.2. Xenolith

E49 contains a spinel–pyroxene-rich inclusion, apparently a xenolithic CAI, distinct from the host CAI (Fig. 2a). The xenolith is composed of two different types of units: (1) fine-grained units with convoluted and symplectitic textures indicative of partial melting in areas close to the interface with the host (Fig. 2d and e) and (2) islands with more blocky minerals in the interior of the xenolith.

The islands consist of fractured and faulted coarse-grained spinel (\pm perovskite \pm FeNi beads, Fig. 2b), associated with gehlenitic melilite (Åk_{10} – Åk_{30}). Clinopyroxene in contact with the islands is Al–Ti-rich. Anorthite is present as thin layers at spinel–pyroxene boundaries. Spinel is corroded and partially replaced

at their surfaces by a symplectite of intergrown spinel and pyroxene at the contact with melilite (Fig. 2c). Symplectite is also present around most spinels in the host, suggesting that they are xenolithic spinels that drifted into the host melt.

While this mineralogy is typical of many CAIs, the mineralogy of the units with convoluted textures is more unusual (Fig. 2d). These units are made up of Ca-rich clinopyroxene, Mg-rich melilite and a fine-grained Ca–Fe–Mg-rich olivine intergrown with a phase darker in backscattered electron images but too small for precise compositional analysis. Finally, a Mg-bearing Si-rich phase with textures of a residual melt is present in some cases (Fig. 2e). Its composition was not determined precisely because it was easily destroyed under the

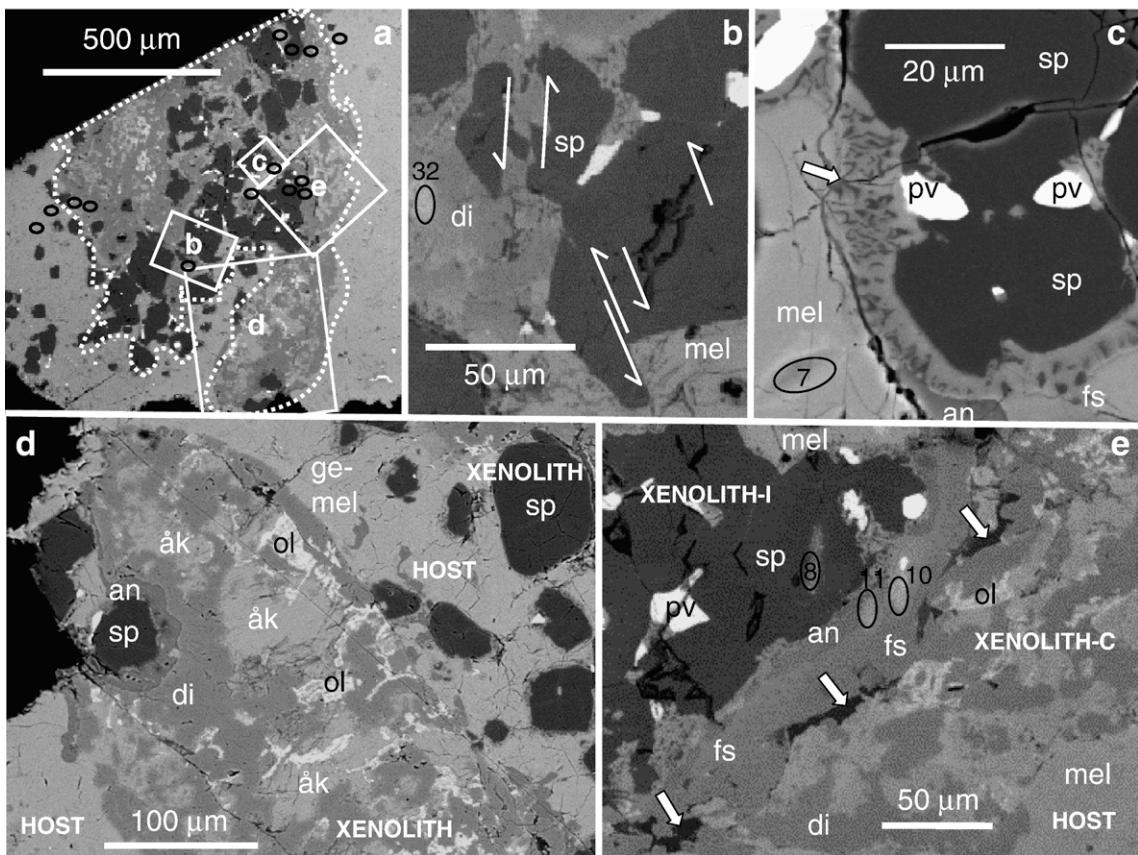


Fig. 2. Backscattered electron (BSE) micrographs of the xenolith inclusion. Abbreviations for all panels are: sp — spinel; an — anorthite; mel — melilite; fs — fassaitic clinopyroxene; di — diopsidic clinopyroxene; pv — perovskite; åk — åkermanite; ge-mel — gehlenitic melilite; ol — olivine. Ion probe pits are indicated with ellipses and numbered according to Table 2. a. General view of the xenolith whose boundary is indicated with dashed contour. Rectangles locate detailed BSE images 2b, c, d and e. b. Coarse-grained fractured spinels. Arrows show the direction of shear fracture along the (111) cleavage plane of spinel. c. Coarse-grained spinels from a relict island corroded by the spinel–pyroxene symplectite (white arrow). d. Droplet-shaped convoluted region of the xenolith intruding into the host. Coarse-grained spinels from the xenolith that drifted into the host melt are visible in the top right portion. The convoluted region is dominated by (Al)–diopside, åkermanite and Fe–monticellite olivine while melilite from the host is gehlenitic. e. Contact between a relict island (xenolith-I) and a convoluted region (xenolith-C). Arrows show the Si-rich phase (dark) with texture of a residual melt at the contact between the island and the convoluted region.

Table 1
Typical chemical analyses of minerals in the convoluted region of the xenolith

| | Fe- monticellite | Fe- monticellite | Fe- monticellite | Fe- monticellite | Fe- monticellite | Melilite | Melilite | Melilite | Melilite | Melilite | Al- diopside | Al- diopside | Al- diopside | Al- diopside | Al- diopside |
|--------------------------------|---------------------|---------------------|---------------------|---------------------|---------------------|----------|----------|----------|----------|----------|-----------------|-----------------|-----------------|-----------------|-----------------|
| SiO ₂ | 35.91 | 35.35 | 39.61 | 36.44 | 35.27 | 43.69 | 43.82 | 44.21 | 43.69 | 43.12 | 54.17 | 54.09 | 54.94 | 55.39 | 54.46 |
| TiO ₂ | 0.00 | 0.02 | 0.00 | 0.00 | 0.05 | 0.03 | 0.00 | 0.01 | 0.03 | 0.00 | 0.06 | 0.01 | 0.02 | 0.24 | 0.02 |
| Al ₂ O ₃ | 0.17 | 0.05 | 0.15 | 0.01 | 0.19 | 0.16 | 0.07 | 0.06 | 0.16 | 1.74 | 0.36 | 0.27 | 0.16 | 1.61 | 2.72 |
| Cr ₂ O ₃ | 0.02 | 0.00 | 0.00 | 0.00 | 0.00 | 0.01 | 0.00 | 0.00 | 0.01 | 0.00 | 0.06 | 0.11 | 0.07 | NA | NA |
| FeO | 18.25 | 20.43 | 15.65 | 19.70 | 18.87 | 0.12 | 0.08 | 0.18 | 0.12 | 0.03 | 0.16 | 0.24 | 0.02 | 0.00 | 0.04 |
| MnO | 0.10 | 0.17 | 0.18 | 0.23 | 0.17 | 0.05 | 0.01 | 0.00 | 0.05 | 0.00 | 0.00 | 0.00 | 0.00 | 0.00 | 0.00 |
| MgO | 11.98 | 11.77 | 12.83 | 11.18 | 12.33 | 14.36 | 14.42 | 14.33 | 14.36 | 13.41 | 18.11 | 18.24 | 18.15 | 18.21 | 17.76 |
| CaO | 32.84 | 31.42 | 30.22 | 32.63 | 31.20 | 39.39 | 40.95 | 40.84 | 39.39 | 40.33 | 25.60 | 26.04 | 25.81 | 26.21 | 26.50 |
| NiO | 0.03 | 0.04 | 0.00 | 0.04 | 0.00 | 0.00 | 0.00 | 0.00 | 0.00 | 0.02 | 0.00 | 0.02 | 0.02 | NA | NA |
| Na ₂ O | 0.03 | 0.00 | 0.03 | 0.05 | 0.01 | 0.00 | 0.03 | 0.03 | 0.00 | 0.10 | 0.00 | 0.00 | 0.01 | 0.07 | 0.24 |
| K ₂ O | 0.00 | 0.01 | 0.01 | 0.00 | 0.00 | 0.00 | 0.00 | 0.00 | 0.00 | 0.01 | 0.00 | 0.00 | 0.00 | 0.01 | 0.01 |
| Total | 99.33 | 99.26 | 98.67 | 100.27 | 98.09 | 97.81 | 99.38 | 99.66 | 97.81 | 98.77 | 98.53 | 99.01 | 99.20 | 101.73 | 101.75 |
| O / formula | 4O | 4O | 4O | 4O | 4O | 7O | 7O | 7O | 7O | 7O | 6O | 6O | 6O | 6O | 6O |
| Si | 1.022 | 1.015 | 1.098 | 1.032 | 1.017 | 2.019 | 2.002 | 2.012 | 2.019 | 1.977 | 1.985 | 1.978 | 1.998 | 1.963 | 1.934 |
| Ti | 0.000 | 0.001 | 0.000 | 0.000 | 0.001 | 0.001 | 0.000 | 0.000 | 0.001 | 0.000 | 0.002 | 0.000 | 0.001 | 0.006 | 0.001 |
| Al | 0.006 | 0.000 | 0.005 | 0.000 | 0.006 | 0.008 | 0.003 | 0.003 | 0.008 | 0.094 | 0.016 | 0.012 | 0.007 | 0.067 | 0.114 |
| Cr | 0.000 | 0.000 | 0.000 | 0.000 | 0.000 | 0.000 | 0.000 | 0.000 | 0.000 | 0.000 | 0.002 | 0.003 | 0.002 | NA | NA |
| FeII | 0.434 | 0.491 | 0.363 | 0.466 | 0.455 | 0.005 | 0.003 | 0.007 | 0.005 | 0.001 | 0.005 | 0.007 | 0.001 | 0.000 | 0.001 |
| Mn | 0.003 | 0.004 | 0.004 | 0.005 | 0.004 | 0.002 | 0.000 | 0.000 | 0.002 | 0.000 | 0.000 | 0.000 | 0.000 | 0.000 | 0.000 |
| Mg | 0.508 | 0.504 | 0.530 | 0.472 | 0.530 | 0.989 | 0.982 | 0.972 | 0.989 | 0.917 | 0.989 | 0.994 | 0.983 | 0.962 | 0.940 |
| Ca | 1.001 | 0.967 | 0.898 | 0.990 | 0.964 | 1.950 | 2.004 | 1.991 | 1.950 | 1.981 | 1.005 | 1.020 | 1.005 | 0.995 | 1.009 |
| Ni | 0.001 | 0.001 | 0.000 | 0.001 | 0.000 | 0.000 | 0.000 | 0.000 | 0.000 | 0.001 | 0.000 | 0.000 | 0.001 | NA | NA |
| Na | 0.001 | 0.000 | 0.001 | 0.003 | 0.001 | 0.000 | 0.002 | 0.003 | 0.000 | 0.009 | 0.000 | 0.000 | 0.000 | 0.005 | 0.016 |
| K | 0.000 | 0.000 | 0.000 | 0.000 | 0.000 | 0.000 | 0.000 | 0.000 | 0.000 | 0.001 | 0.000 | 0.000 | 0.000 | 0.000 | 0.001 |
| Total cations | 2.976 | 2.984 | 2.900 | 2.969 | 2.979 | 4.975 | 4.998 | 4.988 | 4.975 | 4.981 | 4.004 | 4.015 | 3.998 | 3.999 | 4.016 |
| Endmember | Mo 53.9 | Mo 50.7 | Mo 59.4 | Mo 50.3 | Mo 53.8 | Åk 99.6 | Åk 99.8 | Åk 99.8 | Åk 99.6 | Åk 95.1 | | | | | |

NA stands for not analyzed.

electron beam, resulting in very low totals of $\sim 80\%$, suggesting that it is volatile rich. Chemical variations in the convoluted units are small (Table 1). The clinopyroxene is close to pure diopside (Al_2O_3 is mostly below 0.5 wt%, in some cases up to 2.75 wt%), the melilite is close to pure åkermanite ($\text{Åk}_{95}\text{--}\text{Åk}_{100}$) and the Ca–Fe–Mg-rich olivine has a composition close to the middle of the monticellite–kirschsteinite join ($\text{Ca}(\text{Fe}_{0.5}\text{Mg}_{0.5})\text{SiO}_4$). With 50.3–59.4 mol% of the monticellite end-member; we will refer to it as Fe-monticellite rather than Mg-kirschsteinite.

3.2. Trace elements

Trace element patterns were measured in perovskite from the host and the xenolith, in melilite from the host and the xenolith and in clinopyroxene from the xenolith. They are available as supplementary information.

3.2.1. Host

Perovskite is enriched in the Rare Earth Elements (REE) relative to CI abundances by a factor 1000 and has a flat REE pattern with a strong Eu depletion. Light REE in melilite are slightly enriched relative to the heavy REE. A strong Eu excess and possible small excesses in Yb and Lu are observed. These patterns are commonly observed in type A CAIs and are attributed to the fractional crystallization of a Ca–Al-rich melt with melilite crystallizing before perovskite (Simon et al., 1999).

3.2.2. Xenolith

The REE enrichment in perovskite varies from ~ 100 to $1000\times\text{CI}$. One perovskite grain shows a significant fractionation with a steeply rising pattern and heavy REEs being enriched by a factor of 10 relative to the light REEs. All perovskites show strong Eu depletions and moderate Yb excesses. Gehlenitic melilite from an island is enriched in the light REE and has a large Eu excess. Clinopyroxene from the convoluted areas, on the other hand, is slightly enriched in heavy REEs and shows a Yb excess. It lacks the negative Eu anomaly commonly observed in pyroxene from CAIs (MacPherson et al., 1989; Simon et al., 1991, 1999). These patterns are suggestive of crystallization from a melt.

3.3. Oxygen isotopes

We measured oxygen isotopes in spinel from the host, the xenolith and from the Wark–Lovering rim, in pyroxene±anorthite from the xenolith islands and convoluted areas, and in melilite from the host, the xenolith islands and the Wark–Lovering rim (Fig. 3,

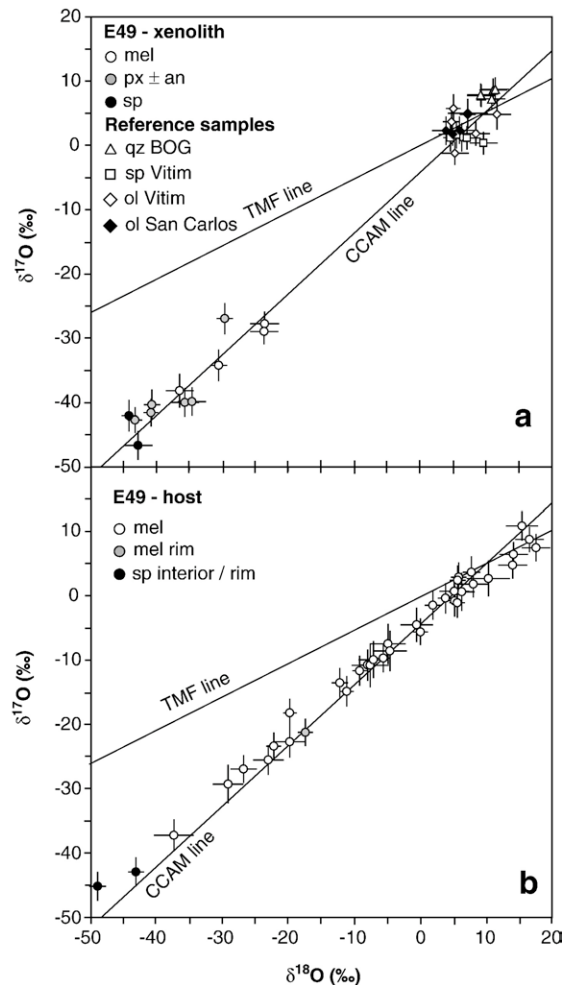


Fig. 3. Oxygen isotopic compositions in E49. All error bars are 2σ and take into account analytical error and uncertainty in instrumental mass fractionation. TMF stands for Terrestrial Mass Fractionation and CCAM for Carbonaceous Chondrite Anhydrous Minerals. a. Oxygen isotopic compositions of minerals in the xenolith and of reference samples used as standards. b. Oxygen isotopic compositions of melilite and spinel in the host and the rim.

Table 2). Two O isotopic traverses in melilite from the host were obtained, starting from the Wark–Lovering rim into the interior (Fig. 1).

3.3.1. Host

Spinel in the host are ^{16}O -rich regardless of their location ($\Delta^{17}\text{O} \leq -19.6 \pm 2.8\text{‰}$, Table 2). Melilite from the WL-rim has intermediate ^{16}O excesses ($\Delta^{17}\text{O} = -12.0 \pm 2.7\text{‰}$, Fig. 3b). In contrast, oxygen isotopic ratios in the host melilite span the whole range of previously reported compositions, $-17.6 \pm 3.5\text{‰} \leq \Delta^{17}\text{O} \leq +3.0 \pm 3.0\text{‰}$. These variations are correlated with the location within the inclusion (Fig. 4a) and with the Åk content of the

Table 2
Oxygen isotope data

| Spot | Mineralogy | Distance from rim (μm) | $\delta^{18}\text{O}$ (‰) ^a | $\delta^{17}\text{O}$ (‰) ^a | $\Delta^{17}\text{O}$ (‰) ^a |
|-----------------|--------------------|--|---|---|---|
| <i>Host</i> | | | | | |
| 12 | Åk _{16.5} | 306 | 5.4±1.1 | -1.0±2.3 | -3.8±2.9 |
| 24 | Åk _{9.7} | 275 | 1.8±1.1 | -1.4±2.1 | -2.3±2.8 |
| 23 | Åk _{11.3} | 256 | 3.6±1.1 | -0.3±2.3 | -2.2±2.9 |
| 22 | Åk _{8.1} | 233 | -8.1±1.1 | -10.6±2.3 | -6.4±2.9 |
| 21 | Åk _{5.5} | 160 | -0.1±1.0 | -5.5±2.0 | -5.4±2.7 |
| 20 | Åk _{11.1} | 137 | -5.7±1.0 | -9.6±2.1 | -6.6±2.7 |
| 19 | Åk _{1.0} | 121 | -9.3±1.0 | -11.5±2.2 | -6.7±2.9 |
| 18 | Åk _{10.1} | 113 | -22.3±1.0 | -23.2±2.0 | -11.6±2.7 |
| 15 | Åk _{2.3} | 92 | -11.2±1.0 | -14.7±2.3 | -8.9±2.9 |
| 17 | Åk _{9.0} | 81 | -12.3±1.2 | -13.4±2.2 | -7.0±2.9 |
| 16 | Åk _{7.7} | 63 | -19.8±0.9 | -18.0±2.1 | -7.7±2.7 |
| 36 | Åk _{5.1} | 111 | -23.1±2.2 | -25.4±2.3 | -13.4±3.1 |
| 37 | Åk _{3.5} | 132 | -37.3±2.9 | -37.0±2.4 | -17.6±3.5 |
| 38 | Åk _{4.2} | 142 | -29.1±2.2 | -29.1±2.9 | -13.9±3.6 |
| 39 | Åk _{7.4} | 165 | -5.0±2.6 | -7.4±3.1 | -4.7±3.8 |
| 40 | Åk _{15.1} | 197 | -7.7±2.7 | -10.7±3.3 | -6.7±4.1 |
| 41 | Åk _{12.2} | 230 | -4.7±2.4 | -8.4±3.1 | -6.0±3.8 |
| 42 | Åk _{4.8} | 150 | -19.8±2.3 | -22.5±2.4 | -12.2±3.2 |
| 43 | Åk _{12.5} | 311 | 5.0±2.2 | 0.8±1.9 | -1.8±2.8 |
| 44 | Åk _{7.1} | 158 | -26.8±1.9 | -26.8±2.1 | -12.8±2.8 |
| 45 | Åk _{12.2} | 178 | -7.2±2.2 | -9.8±2.8 | -6.1±3.5 |
| 46 | Åk _{11.2} | 285 | -0.7±2.4 | -4.4±2.6 | -4.0±3.4 |
| 35 | Åk _{25.8} | 1777 | 5.6±1.1 | 3.0±2.2 | 0.0±2.9 |
| 2 | mel | 831 | 16.3±2.1 | 8.8±1.9 | 0.4±3.2 |
| 1 | Åk _{27.9} | 692 | 17.3±2.1 | 7.6±2.0 | -1.4±3.3 |
| 5 | mel | 1892 | 7.8±2.1 | 1.9±2.0 | -2.2±3.3 |
| 3 | mel | 865 | 13.8±2.1 | 4.9±2.0 | -2.3±3.3 |
| 4 | Åk _{23.8} | 1938 | 13.9±2.1 | 6.5±1.9 | -0.7±3.2 |
| 25 | mel | 796 | 5.0±1.1 | -0.7±2.4 | -3.3±3.0 |
| 26 | mel | 842 | 7.6±1.2 | 3.8±2.4 | -0.2±3.0 |
| 30 | Åk _{29.9} | 1015 | 5.5±1.1 | 2.5±2.2 | -0.3±2.8 |
| 47 | mel | 692 | 10.1±3.2 | 2.8±2.7 | -2.5±3.8 |
| 48 | mel | 796 | 6.1±1.8 | 0.7±2.9 | -2.5±3.4 |
| 49 | mel | 1938 | 15.2±2.3 | 10.9±2.2 | 3.0±3.0 |
| 27 | sp | 854 | -48.8±1.1 | -44.9±2.2 | -19.6±2.8 |
| <i>Rim</i> | | | | | |
| 13 | sp | | -43.0±1.1 | -42.7±2.2 | -20.4±2.8 |
| 14 | Åk _{17.3} | | -17.5±1.1 | -21.1±2.0 | -12.0±2.7 |
| <i>Xenolith</i> | | | | | |
| 6 | Åk _{21.2} | | -23.6±2.1 | -27.7±1.8 | -15.4±3.2 |
| 7 | Åk _{18.4} | | -23.7±2.1 | -28.9±1.9 | -16.6±3.3 |
| 31 | Åk _{22.5} | | -30.6±1.2 | -34.2±2.4 | -18.3±3.0 |
| 50 | mel | | -36.5±2.0 | -38.1±2.6 | -19.1±3.2 |
| 32 | cpx | | -29.7±1.2 | -26.9±2.2 | -11.5±2.9 |
| 33 | cpx | | -43.3±1.0 | -42.7±2.4 | -20.2±3.0 |
| 34 | cpx | | -40.9±1.0 | -41.6±2.1 | -20.3±2.8 |
| 10 | cpx | | -35.8±2.1 | -40.0±2.2 | -21.4±3.4 |
| 11 | cpx | | -34.7±2.1 | -39.8±2.2 | -21.8±3.4 |
| 29 | cpx | | -40.8±1.1 | -40.3±2.3 | -19.1±2.9 |
| 8 | sp | | -42.9±2.1 | -46.7±2.2 | -24.4±3.4 |
| 28 | sp | | -44.2±1.1 | -42.0±2.4 | -19.0±3.0 |

Abbreviations: Åk: Åkermanite content in melilite, mel: melilite whose Åk content was not measured, sp: spinel, cpx: Al–Ti-rich clinopyroxene.

^a Errors are 2 σ (95% confidence interval).

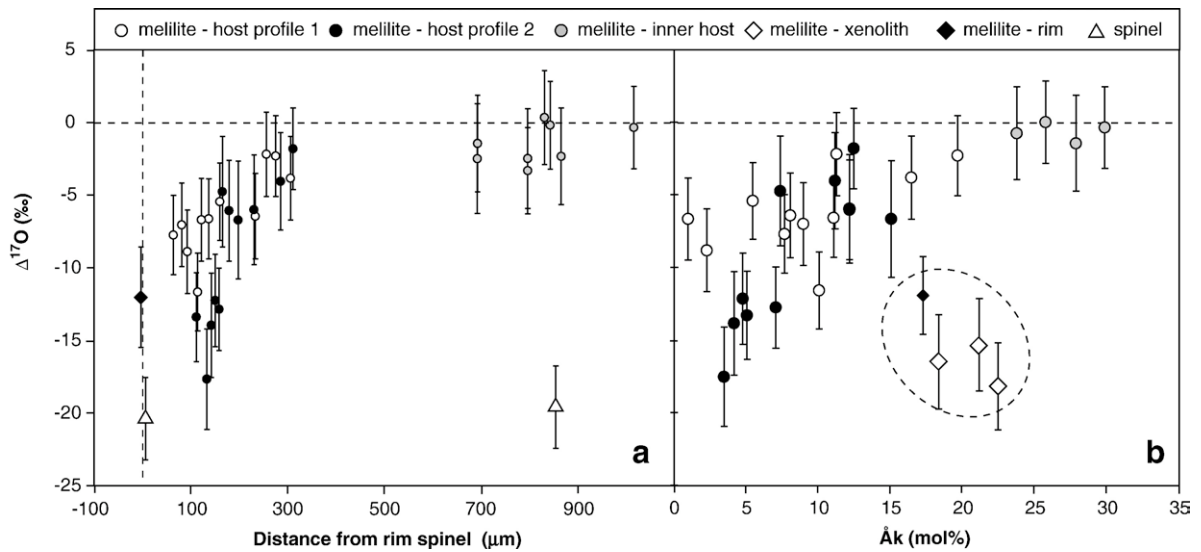


Fig. 4. Oxygen isotopic deviations from the terrestrial mass fractionation line in melilite and spinel. Error bars are 2σ . a. $\Delta^{17}\text{O}$ as a function of distance to the rim. b. $\Delta^{17}\text{O}$ of melilite as a function of Åk content. Melilite from the rim and the xenolith are grouped in the encircled area.

melilite (Fig. 4b). Immediately below the WL-rim, melilite is ^{16}O -rich gehlenite (down to Åk₁), but the ^{16}O -excess decreases towards the center of the inclusion while the Åk content increases up to Åk_{20–30}.

3.3.2. Xenolith

In the xenolith (Fig. 3a), spinel is ^{16}O -rich ($\Delta^{17}\text{O} \leq 19.0 \pm 3.0\text{‰}$), pyroxene with convoluted textures is simi-

larly ^{16}O -rich ($\Delta^{17}\text{O} \leq -19.1 \pm 2.9\text{‰}$), with the exception of one spot ($\Delta^{17}\text{O} = -11.5 \pm 2.9\text{‰}$), and gehlenitic melilite is enriched in ^{16}O to varying degrees ($-19.1 \pm 3.2\text{‰} \leq \Delta^{17}\text{O} \leq -15.4 \pm 3.2\text{‰}$). The ^{16}O -rich convoluted pyroxene from the xenolith is in close contact with ^{16}O -poor melilite from the host (e.g., spots 34 and 35, 20 μm away from each other, have a 20.3‰ difference in $\Delta^{17}\text{O}$, Table 2).

Table 3
Magnesium isotope data

| Spot | Mineralogy | Al/ ²⁴ Mg ^a | ²⁶ Mg/ ²⁴ Mg ^a | F _{Mg} (‰/amu) ^a |
|--------------------|---------------------------|-----------------------------------|---|---|
| Sp-1a | sp, xen | 2.68±0.06 | 0.13953±0.00026 | 0.8±2.6 |
| Sp-1b | sp, xen | 2.81±0.06 | 0.13933±0.00026 | 2.3±2.6 |
| Sp-2 | sp, host | 2.71±0.06 | 0.13964±0.00044 | 1.0±3.2 |
| Sp-3 | sp, rim | 2.81±0.08 | 0.13958±0.00026 | 1.2±2.4 |
| Sp-4 | sp, rim | 3.12±0.06 | 0.13965±0.00028 | 0.8±2.4 |
| Sp-5 | sp, xen | 2.79±0.04 | 0.13982±0.00028 | -0.3±2.6 |
| Sp-6 | sp, xen | 2.79±0.04 | 0.13967±0.00030 | -0.9±2.8 |
| An-1 | an, xen | 10.01±0.48 | 0.13960±0.00064 | 0.4±4.6 |
| Mel-1 | mel, host | 22.45±0.41 | 0.14056±0.00036 | 1.6±2.6 |
| Mel-2 | mel, host–xen boundary | 12.81±0.33 | 0.14006±0.00052 | 1.3±2.8 |
| Mel-3 | mel, host–xen boundary | 9.51±0.17 | 0.13991±0.00030 | 0.9±2.6 |
| Mel-4 | mel, xen | 15.26±0.30 | 0.13992±0.00038 | 1.1±2.8 |
| Mel-5 ^b | Åk _{28.2} , host | 7.69±0.17 | 0.13956±0.00030 | 3.5±2.6 |
| Mel-6 ^b | Åk _{18.6} , host | 13.44±0.22 | 0.13991±0.00022 | 4.0±2.6 |
| Mel-7 ^b | Åk _{7.5} , host | 26.01±0.34 | 0.14045±0.00056 | 2.1±2.6 |
| Dio-1 | cpx, xen | 0.121±0.004 | 0.13952±0.00032 | 2.4±2.6 |
| Dio-2 | cpx, xen | 0.060±0.002 | 0.13931±0.00026 | 3.1±2.6 |

Abbreviations: Åk: Åkermanite content in melilite, mel: melilite whose Åk content was not measured, sp: spinel, cpx: Al–Ti-rich clinopyroxene, xen: xenolith.

^a Errors are 2σ (95% confidence interval).

^b Spots 5–7 define a profile parallel to the O isotope traverse 1, spot 5 is in the inner host, spot 6 is located ~80 μm inwards beyond the end of the O isotope traverse 1 and spot 7 is located close to the middle of O isotope traverse 1.

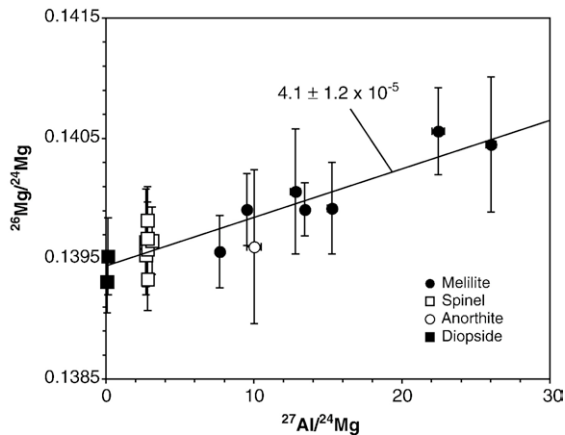


Fig. 5. $^{26}\text{Mg}/^{24}\text{Mg}$ ratios as a function of Al^{24}Mg ratios. The data from both the host and the xenolith define an isochron whose slope gives an initial $^{26}\text{Al}/^{27}\text{Al}$ ratio of $4.1 \pm 1.2 \times 10^{-5}$ for the closure of the Mg isotope system.

3.4. Magnesium isotopes

Magnesium isotopes were measured in pyroxene from the xenolith and in spinel and melilite from the host and the xenolith (Table 3 and supplementary information). Both inclusions have a similar Mg isotope distribution with almost no mass fractionation relative to a terrestrial reference ($-1\% < F_{\text{Mg}} < 4\%$). Although no analysis of gehlenite was obtained at the contact with the rim, three measurements along oxygen isotope traverse 1 show no resolvable F_{Mg} differences for melilite with Mg content varying from $\text{Åk}_{28.2}$ to $\text{Åk}_{7.5}$ (Table 3). ^{26}Mg excesses are present in the host and the xenolith and can be attributed to the in-situ decay of ^{26}Al . The inferred initial $^{26}\text{Al}/^{27}\text{Al}$ ratio for both inclusions is canonical within error at $4.1 \pm 1.2 \times 10^{-5}$ (Fig. 5).

4. Discussion

4.1. Relationship between the host and the xenolith

Because of the temperature minimum in the phase diagram of melilite at $\sim \text{Åk}_{73}$ (e.g., Mendybaev et al., 2006), the striking compositional difference between melilite in the convoluted area of the xenolith ($\sim \text{Åk}_{100}$) and the adjacent host ($\sim \text{Åk}_{30}$) clearly indicates that these melilite phases crystallized from two different melts that barely interacted with each other. Åkermanitic melilite from the xenolith apparently crystallized from a very Mg-rich melt, whereas melilite from the host crystallized from an Al-rich melt typical of compact type A CAIs (Simon et al., 1999). The presence of islands of gehlenitic melilite

in the xenolith suggests that they are relicts from a previous generation of crystals in the xenolith that did not remelt during the injection into the host.

The presence of Fe-monticellite in the convoluted regions of the xenolith is equally indicative of limited interactions between the host melt and the xenolith melt because its formation requires a melt with a locally high enough $f\text{O}_2$ value to have Fe incorporated as FeO in the silicates rather than being present as Fe metal such as observed in both the host and the xenolith islands. Therefore, the presence of Fe-monticellite is best explained by the crystallization of a locally oxidizing melt produced by the melting of a Fe-bearing silicate. This crystallization from a melt together with the lack of extensive alteration in the host requires that the Fe-oxidizing alteration event occurred in the protosolar nebula before the collision between the host and the xenolith.

The convoluted texture of the pyroxene associated with Åkermanitic melilite suggests that the xenolith was partially crystallized while the host was more extensively molten. Its ^{16}O -rich composition also agrees with a lack of interaction between the host melt and the xenolith partial melt.

Some interaction between the host melt and the xenolith partial melt is nevertheless indicated by one spot in the pyroxene with an intermediate O isotopic composition (spot 32, Table 2), the observation of Åk_{75} at the contact between xenolith Åkermanite and host gehlenitic melilite, and the observation of a minute metal grain embedded in Fe-monticellite, probably due to reduction by the low $f\text{O}_2$ of the host.

Spinel from the xenolith are dominantly broken and partially faulted, indicating that they were fractured but not molten during the injection of the xenolith. Thus, they kept the ^{16}O -rich composition of the xenolith precursor. The presence of the spinel–pyroxene symplectite and textures of spinel corrosion at the spinel–melilite interface are indicative of limited spinel melting. The intermediate O isotopic composition of the melilite islands suggest that also they were initially ^{16}O -rich and experienced solid-state diffusion of ^{16}O -poor oxygen from the ^{16}O -poor host or minor partial melting and recrystallization. The systematically ^{16}O -rich composition of the xenolith, together with evidence of minor interactions with a ^{16}O -poor reservoir suggests that the xenolith precursor was uniformly ^{16}O -rich and was injected into a dominantly ^{16}O -poor CAI liquid.

The lack of extensive oxygen isotopic re-equilibration suggests together with the petrographic evidence of limited interactions that the injection occurred during cooling of the host CAI, shortly before it was fully crystallized. Therefore, all petrographic, chemical and

isotopic observations point toward formation of the compound inclusion by impact of a Mg-rich, ^{16}O -rich CAI, previously altered in the nebula, into an extensively molten, ^{16}O -depleted, type A host CAI shortly before the host's final crystallization. Convoluted regions in the xenolith were probably formed by the rapid crystallization of the partial melt produced during impact, possibly owing to the presence of altered phases with melting points lower than the temperature of the host.

4.2. Oxygen isotope exchange during fractional crystallization of the host CAI

Oxygen isotope profiles starting from the exterior towards the interior of the host CAI show a progressive ^{16}O depletion associated with Mg enrichment of melilite, which suggests that the oxygen isotopic variations are associated with the crystallization of the outer melilite layer. In the following, we distinguish between the initial crystallization of a dominantly molten inclusion in a cooling gaseous reservoir and the late recrystallization of the outer portion of a solid CAI after partial melting by a brief heating event.

In contrast to previous observations of O isotope variations in zoned melilite and anorthite crystals (Yurimoto et al., 1998; Itoh and Yurimoto, 2003; Yoshitake et al., 2005), the O isotope profiles in E49 cannot be attributed to recrystallization of melilite after a late remelting event. Indeed, if ^{16}O -rich gehlenite formed by remelting of ^{16}O -poor melilite with high Mg content (Åk_{20-30}) during a high temperature event, a loss of at least 75% of the Mg would be required. However the absence of Mg isotopic fractionation ($F_{\text{Mg}} \leq 3 \pm 2\%$, where F_{Mg} is the spread in the $\delta^{25}\text{Mg}$ values measured near the O isotope traverse) indicates the absence of Rayleigh isotopic fractionation due to loss of Mg by evaporation from a molten outer region.

Correlated solid-state diffusion of O and Mg during a late reheating event is also unlikely. Although the O isotope profiles could be the result of solid-state diffusion, the self-diffusion of O in gehlenite (Yurimoto et al., 1989; Ryerson and McKeegan, 1994) is slow and would require temperatures as high as the crystallization temperature of Åk_{20} (1700 K, Stolper, 1982) for roughly 10–100 yr to fit the observed profiles. Such a high temperature likely would have resulted in partial melting. Moreover, such extensive heating would have resulted in partial equilibration of the CAI's Mg content due to self-diffusion of Mg in melilite (LaTourrette and Hutcheon, 1999). As a consequence, gehlenite could not be present in a CAI dominated by Åk_{20-30} melilite without

significant Mg loss, for which there is no evidence in E49, because of the absence of Mg isotopic fractionation.

Finally, Fe–alkali metasomatism has also been proposed as a mechanism for oxygen isotope exchange in CAIs from metamorphosed chondrites (Wasson et al., 2001). Although this process also requires mineral transformations and cannot be responsible for isotope exchange in coarse-grained CAI from mostly reduced meteorites, such as E49, the intermediate O isotopic composition of melilite from the WL-rim (Fig. 4) is probably due to diffusion of parent-body oxygen during the geological activity of the parent-body, owing to the fine-grained texture of the rim (Aléon et al., 2005; Yoshitake et al., 2005).

Oxygen isotopic variations were thus probably acquired during the initial crystallization of the inclusion. Both the Rare Earth Element patterns and the chemical zonation of melilite, with gehlenitic compositions near the surface of the inclusion and a steady increase in Åk content towards the interior, are suggestive of fractional crystallization from a melt (MacPherson et al., 1989; Simon et al., 1999) starting from the surface. We thus propose two hypotheses. In the first hypothesis, an ^{16}O -rich melt diffusively equilibrated with an ^{16}O -poor gas before the end of crystallization. In this scenario, O was transported by diffusion in the liquid between the growing crystals (Fig. 6a). A comparison of the relative timescales for diffusion and crystallization lends support to this hypothesis. Diffusion of O through a 300 μm thick layer of Ca–Al-rich melt (Oishi et al., 1974) yields the observed depletion in ^{16}O in as little as ~ 5 s, while the inner melilite (Åk_{20-30}) starts to crystallize ~ 5 –200 h after the outer melilite (Åk_1) at typical CAI cooling rates of 0.5 K/h–20 K/h (Stolper, 1982; Paque and Stolper, 1984; Stolper and Paque, 1986). In the second hypothesis, the host melt was ^{16}O -poor and entered a ^{16}O -rich gas at the onset of crystallization of the outer layers. The first crystallizing melilite quickly acted as a physical barrier to diffusion, maintaining the ^{16}O -poor composition in the interior of the CAI during the final stages of cooling (Fig. 6b). This scenario is supported by the observation of ^{16}O excesses in the WL-rim. Hypothesis 1 seems to be more likely based on diffusion kinetics but hypothesis 2 agrees better with the petrography. On the basis of the present data it is thus difficult to decide which interpretation is correct. However, in both hypotheses the correlation between O isotopic composition and Mg content of the melilite requires that the oxygen isotope exchange took place during fractional crystallization of the outer layer of the CAI, i.e., on a time scale of 5–200 h.

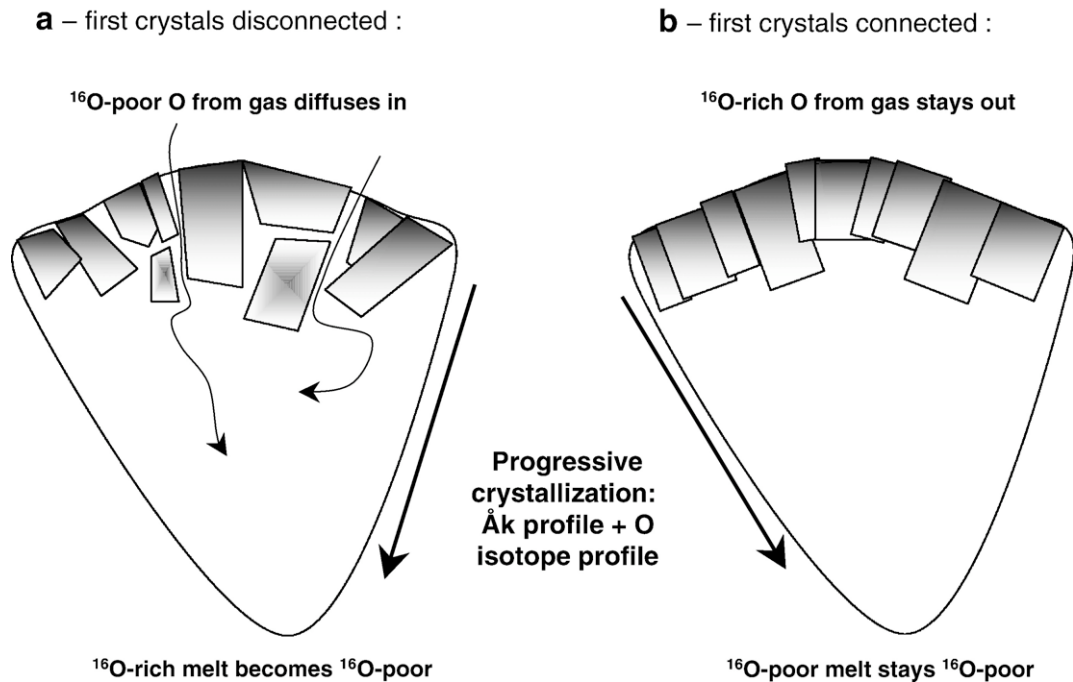


Fig. 6. Schematics of the two scenarii that explain the oxygen isotope data in E49. These two scenarii are distinguished by the nucleation mechanism of the first crystals formed at the edge of the inclusion. a. If the first crystals are disconnected, the fast kinetics of oxygen diffusion in the interstitial melt allows isotopic equilibration of the interior with the gas. b. If the first crystals are connected, they act as a protective layer that prevents equilibration of the interior with the gas.

4.3. Evidence for early isotopic heterogeneities in the protosolar nebula

We conclude that the oxygen isotopic zoning observed in E49 reflects the change in the oxygen isotopic composition of the gas during fractional crystallization of the host inclusion. A period of 5–200 h seems to be too short to allow the oxygen isotopic composition of a particular nebular region to change by 5%. It is thus likely that the CAI crystallization occurred during transport between two isotopically distinct nebular regions. Stellar winds, such as X-winds, provide a setting for melting and large-scale transport of CAIs at high temperature and high speed (Shu et al., 1997). At typical X-wind speed (200 km s^{-1} , Shu et al., 1997) the distance covered in 5–200 h is at most 1 AU. However a significant amount of evaporation should occur under such conditions, which is not observed in E49. Transport at higher pressures within the accretion disk, e.g. by turbulence, would happen at low speeds, resulting in distances on the order of 10^4 – 10^5 km (Ciesla, pers. comm.), which is small compared to the expected scale of nebular isotopic heterogeneities. While the exact transport mechanism remains to be determined, the isotopic zoning of E49 combined with crystallization

time and speeds on the order of 10 – 50 km s^{-1} would result in a reasonable scale for isotopic variations in the nebula (Fig. 7). In order for the two CAIs to be preserved upon impact, the relative speeds of the two inclusions must have been small. This suggests that the impact occurred during the cooling and the slowing of the host after it encountered the second nebular reservoir, which is in agreement with the petrographic and isotopic observations that the xenolith impacted a dominantly ^{16}O -poor host shortly before the end of the latter's crystallization. The short timescale implied by this scenario is consistent with the lack of any difference in the initial $^{26}\text{Al}/^{27}\text{Al}$ ratio between the host and the xenolith.

The initial $^{26}\text{Al}/^{27}\text{Al}$ ratio determined from the measurements of melilite is $4.1 \pm 1.2 \times 10^{-5}$ (2σ , Fig. 5). With an initial Solar System $^{26}\text{Al}/^{27}\text{Al}$ ratio of 5.85×10^{-5} , (Thrane et al., 2006), this corresponds to an age of crystallization of E49 of $370,000 \pm 300,000$ (2σ) years after the birth of the Solar System. This age corresponds to the last crystallization event of E49 when the xenolith was captured, and does not preclude repeated melting events after the formation of their precursor materials and before this event. We note that our minimum age estimate of 70,000 yr is in agreement

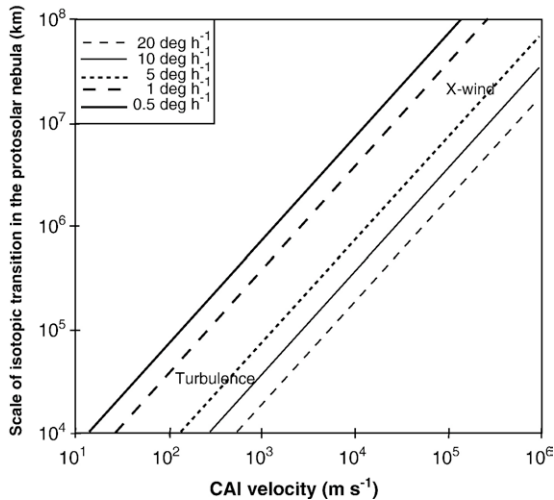


Fig. 7. Scale of oxygen isotopic transition in the protosolar nebula gas as function of CAI velocities for several cooling rates. The cooling rate (in K/h) determines the time interval between crystallization of gehlenite and Åk_{30} (at temperatures that differ by ~ 100 K), which occur in two reservoirs with different oxygen isotopic composition. The distance traversed by the CAI during this time interval is indicative of the spatial scale of the O isotopic transition in the protosolar nebula gas. Typical velocities due to turbulence and the X-wind are indicated for reference and provide lower and upper limits, respectively.

with the maximum duration of CAI precursor formation of 100,000 yr (Thrane et al., 2006). Thus large parts of the protosolar nebula had an oxygen isotope difference $\geq 5\%$ relative to each other at most 670,000 yr after the onset of Solar System formation and possibly since the beginning. In a scenario, where an initial ^{16}O -rich nebula i.e. a ^{16}O -rich presolar molecular cloud became ^{16}O -poor, this evolution would have taken less than half the time than previously thought (Krot et al., 2005b). This time constraint for the nebula is consistent with dynamic calculations, which indicate that Moon- to Mars-sized planetary embryos formed within the first few 10^5 yr of existence of the Solar System by rapid runaway growth (e.g., Chambers, 2004). Our investigation shows that the solar nebula had a reservoir with the right oxygen isotopic composition to build such planetesimals at a time when large amounts of ^{26}Al provided the heat for rapid differentiation. This conclusion is in agreement with the finding that the parent planetesimal of the differentiated angrite meteorites might have formed less than 1 Myr after CAI formation (Baker et al., 2005). Alternatively, our results are in good agreement with the proposal that the Sun, and thus most of the protosolar nebula, has the terrestrial O isotopic composition (Ozima et al., 2007). In such a case, the ^{16}O -rich reservoir would be secondary and of limited spatial extent. In this case,

the self-shielding model would not be appropriate to describe the O isotopic evolution of the solar nebula.

5. Conclusions

Efremovka inclusion E49 is a complex compound CAI formed by the impact of a ^{16}O -rich Mg-rich CAI that had experienced nebular oxidizing alteration into a zoned compact type A CAI. Melilite in the first $300\ \mu\text{m}$ at the periphery of the host CAI is ^{16}O -rich gehlenite that shows a progressive enrichment in Mg correlated with a depletion in ^{16}O toward the interior. In the absence of Mg isotope fractionation, this oxygen isotopic zoning is best attributed to isotope exchange during fractional crystallization of the host inclusion. The short timescale for this event (a few tens of hours) implies that the host CAI encountered two gaseous reservoirs with different oxygen isotopic compositions during the crystallization of its outer portion. Al/Mg isotopes revealed that these two reservoirs co-existed shortly after CAIs with the canonical $^{26}\text{Al}/^{27}\text{Al}$ ratio formed, at most 670,000 yr after the birth of the Solar System. We thus showed that both a ^{16}O -rich reservoir with a composition typical of CAI spinels and a ^{16}O -poor reservoir with planetary isotopic composition co-existed very early in the protosolar nebula. Models postulating the transformation of an initial ^{16}O -rich gas into the planetary oxygen reservoir have to account for such a rapid evolution. The existence of a reservoir with the right oxygen isotopic composition to build planetesimals early, when enough ^{26}Al was available to provide the heat for rapid differentiation is in agreement with dynamic calculations indicating the rapid accretion of Moon- to Mars-sized planetary embryos. The systematics of oxygen isotope variations in E49 thus indicates that the nebular ^{16}O -rich reservoir was of limited spatial extent early in our Solar System history and did not prevent rapid accretion and differentiation of planetesimals in the protosolar nebula in a homogeneous ^{16}O -poor reservoir.

Acknowledgements

JA would like to thank A. Toppani, P. Barbey and F. Ciesla for the discussions and I. D. Hutcheon for the comments. We would like to thank Dr. Richard W. Carlson for editorial work and Dr. Alexander N. Krot and an anonymous reviewer for constructive reviews. This work was supported by PNP-INSU grants and the Région Lorraine (O isotopes) and by NASA grant NNG04GG49G (Mg isotopes and trace elements). This is CRPG-CNRS contribution n° 1880.

Appendix A. Supplementary data

Supplementary data associated with this article can be found, in the online version, at [doi:10.1016/j.epsl.2007.09.003](https://doi.org/10.1016/j.epsl.2007.09.003).

References

- Aléon, J., Krot, A.N., McKeegan, K.D., MacPherson, G.J., Ulyanov, A.A., 2005. Fine-grained, spinel-rich inclusions from the reduced CV chondrite Efremovka: II. Oxygen isotopic composition. *Meteorit. Planet. Sci.* 40, 1043–1058.
- Amelin, Y., Krot, A.N., Hutcheon, I.D., Ulyanov, A.A., 2002. Lead isotopic ages of chondrules and calcium–aluminum-rich inclusions. *Science* 297, 1678–1683.
- Baker, J., Bizzarro, M., Wittig, N., Connelly, J., Haack, H., 2005. Early planetesimal melting from an age of 4.5662 Gyr for differentiated meteorites. *Nature* 436, 1127–1131.
- Chambers, J.E., 2004. Planetary accretion in the inner Solar System. *Earth Planet. Sci. Lett.* 223, 241–252.
- Clayton, R.N., 1993. Oxygen isotopes in meteorites. *Annu. Rev. Earth Planet. Sci.* 21, 115–149.
- Clayton, R.N., 2002. Self-shielding in the solar nebula. *Nature* 415, 860–861.
- Clayton, R.N., 2004. Oxygen isotopes in meteorites. In: Davis, A.M. (Ed.), *Treatise on Geochemistry. Meteorites, Comets and Planets*, vol. 1. Elsevier, Oxford, pp. 129–141.
- Clayton, R.N., Grossman, L., Mayeda, T.K., 1973. A component of primitive nuclear composition in carbonaceous meteorites. *Science* 182, 485–487.
- Clayton, R.N., Onuma, N., Grossman, L., Mayeda, T.K., 1977. Distribution of the presolar component in Allende and other carbonaceous chondrites. *Earth Planet. Sci. Lett.* 34, 209–224.
- El Goresy, A., Zinner, E.K., 1994. Efremovka E49: a compact type-A CAI containing a partially molten spinel–melilite–diopside xenolith. *Meteoritics* 29, 461–462.
- Grossman, L., 1972. Condensation in the primitive solar nebula. *Geochim. Cosmochim. Acta* 36, 597–619.
- Hashizume, K., Chaussidon, M., 2005. A non-terrestrial ^{16}O -rich isotopic composition for the protosolar nebula. *Nature* 434, 619–622.
- Ireland, T., Holden, P., Norman, M.D., Clarke, J., 2006. Isotopic enhancements of ^{17}O and ^{18}O from solar wind particles in the lunar regolith. *Nature* 440, 776–778.
- Ireland, T.R., Holden, P., Norman, M.D., Mya, J., Asplund, M., 2007. Soils ain't soils: the preservation of solar wind in metal grains from the lunar regolith (abstract). *Lunar Planet. Sci.* 38, 1449.
- Itoh, S., Yurimoto, H., 2003. Contemporaneous formation of chondrules and refractory inclusions in the early Solar System. *Nature* 423, 728–731.
- Jones, R.H., Leshin, L.A., Guan, Y., Sharp, Z.D., Durakiewicz, T., Schilk, A.J., 2004. Oxygen isotope heterogeneity in chondrules from the Mokoia CV3 carbonaceous chondrite. *Geochim. Cosmochim. Acta* 68, 3423–3438.
- Kim, G.L., Yurimoto, H., Sueno, S., 2002. Oxygen isotopic composition of a compound Ca–Al-rich inclusion from Allende meteorite: implications for origin of palisade bodies and O-isotopic environment in the CAI forming region. *J. Mineral. Petrol. Sci.* 97, 161–167.
- Kobayashi, S., Imai, H., Yurimoto, H., 2003. New extreme ^{16}O -rich reservoir in the early Solar System. *Geochim. J.* 37, 663–669.
- Krot, A.N., McKeegan, K.D., Leshin, L.A., MacPherson, G.J., Scott, E.R.D., 2002. Existence of an ^{16}O -rich gaseous reservoir in the solar nebula. *Science* 295, 1051–1054.
- Krot, A.N., Yurimoto, H., Hutcheon, I.D., MacPherson, G.J., 2005a. Chronology of the early Solar System from chondrule-bearing calcium–aluminum-rich inclusions. *Nature* 434, 998–1001.
- Krot, A.N., Hutcheon, I.D., Yurimoto, H., Cuzzi, J.N., McKeegan, K.D., Scott, E.R.D., Libourel, G., Chaussidon, M., Aléon, J., Petaev, M., 2005b. Evolution of oxygen isotopic composition in the inner solar nebula. *Astrophys. J.* 622, 1333–1342.
- LaTourrette, T., Hutcheon, I.D., 1999. Mg diffusion in melilite: thermal histories for CAIs and their parent bodies (abstract). *Lunar Planet. Sci.* 30, 2003.
- Lyons, J.R., Young, E.D., 2005. CO self-shielding as the origin of oxygen isotope anomalies in the early solar nebula. *Nature* 435, 317–320.
- MacPherson, G.J., 2004. Calcium-aluminum-rich inclusions in chondritic meteorites. In: Davis, A.M. (Ed.), *Treatise on Geochemistry. Meteorites, Comets and Planets*, vol. 1. Elsevier, Oxford, pp. 201–246.
- MacPherson, G.J., Crozaz, G., Lundberg, L., 1989. The evolution of a complex type B Allende inclusion: an ion microprobe trace element study. *Geochim. Cosmochim. Acta* 53, 2413–2427.
- Marcus, R.A., 2004. Mass-independent isotope effect in the earliest processed solids in the Solar System: a possible chemical mechanism. *J. Chem. Phys.* 121, 8201–8211.
- McKeegan, K.D., Leshin, L.A., 2001. Stable isotope variations in extraterrestrial materials. In: Valley, J.W., Cole, D.R. (Eds.), *Stable Isotope Geochemistry. Reviews in Mineralogy and Geochemistry*, vol. 43. Mineralogical Society of America, Washington, pp. 279–318.
- Mendybaev, R.A., Richter, F.M., Davis, A.M., 2006. Reevaluation of the åkermanite–gehlenite binary system (abstract). *Lunar Planet. Sci.* 37, 2268.
- Nuth III, J.A., Kimura, Y., Thieme, M.H., Chakraborty, S., 2006. Non-mass dependent oxygen isotopic fractionation of refractory oxide dust produced in an electrical discharge (abstract). *Lunar Planet. Sci.* 37, 1077.
- Oishi, Y., Terai, R., Ueda, H., 1974. Oxygen diffusion in liquid silicates and relation to their viscosity. In: Cooper, A.R., Heuer, A.H. (Eds.), *Mass Transports in Ceramics*. Plenum Press, New York, pp. 297–310.
- Ozima, M., Podosek, F.A., Higuchi, T., Yin, Q.Z., Yamada, A., 2007. On the mean oxygen isotope composition of the Solar System. *Icarus* 186, 562–570.
- Paque, J.M., Stolper, E., 1984. Crystallization experiments on a range of Ca–Al-rich inclusion compositions. *Proc. Lunar Planet. Sci. Conf.* 15th, pp. 631–632.
- Robert, F., 2004. The common property of isotopic anomalies in meteorites. *Astron. Astrophys.* 415, 1167–1176.
- Ryerson, F.J., McKeegan, K.D., 1994. Determination of oxygen self-diffusion in åkermanite, anorthite, diopside, and spinel: implications for oxygen isotopic anomalies and the thermal histories of Ca–Al-rich inclusions. *Geochim. Cosmochim. Acta* 58, 3713–3734.
- Scott, E.R.D., Krot, A.N., 2001. Oxygen isotopic compositions and origins of calcium-aluminum-rich inclusions and chondrules. *Meteorit. Planet. Sci.* 36, 1307–1319.
- Shu, F.H., Shang, H., Glassgold, A.E., Lee, T., 1997. X-rays and fluctuating X-winds from protostars. *Science* 277, 1475–1479.
- Simon, S.B., Grossman, L., Davis, A.M., 1991. Fassaite composition trends during crystallization of Allende Type B refractory inclusion melts. *Geochim. Cosmochim. Acta* 55, 2635–2655.
- Simon, S.B., Davis, A.M., Grossman, L., 1999. Origin of compact type A refractory inclusions from CV3 carbonaceous chondrites. *Geochim. Cosmochim. Acta* 63, 1233–1248.

- Stolper, E., 1982. Crystallization sequences of Ca–Al-rich inclusions from Allende: an experimental study. *Geochim. Cosmochim. Acta* 46, 2159–2180.
- Stolper, E., Paque, J., 1986. Crystallization sequences of Ca–Al-rich inclusions from Allende: the effects of cooling rate and maximum temperature. *Geochim. Cosmochim. Acta* 50, 1785–1806.
- Thiemens, M.H., Heidenreich III, J.E., 1983. The mass-independent fractionation of oxygen: a novel isotope effect and its possible cosmochemical implications. *Science* 219, 1073–1074.
- Thrane, K., Bizzaro, M., Baker, J.A., 2006. Extremely brief formation interval for refractory inclusions and uniform distribution of ^{26}Al in the early Solar System. *Astrophys. J.* 646, L159–L162.
- Wark, D.A., Lovering, J.F., 1977. Marker events in the early evolution of the Solar System: evidence from rims on Ca–Al-rich inclusions in carbonaceous chondrites. *Proc. Lunar Sci. Conf.* 8th, pp. 95–112.
- Wasson, J.T., Yurimoto, H., Russell, S.S., 2001. ^{16}O -rich melilite in CO3.0 chondrites: possible formation of common, ^{16}O -poor melilite by aqueous alteration. *Geochim. Cosmochim. Acta* 65, 4539–4549.
- Yoshitake, M., Koide, Y., Yurimoto, H., 2005. Correlations between oxygen-isotopic composition and petrologic setting in a coarse-grained Ca, Al-rich inclusion. *Geochim. Cosmochim. Acta* 69, 2663–2674.
- Yurimoto, H., Kuramoto, K., 2004. Molecular cloud origin for the oxygen isotope heterogeneity in the Solar System. *Science* 305, 1763–1766.
- Yurimoto, H., Morioka, M., Nagasawa, H., 1989. Diffusion in single crystals of melilite: I. Oxygen. *Geochim. Cosmochim. Acta* 53, 2387–2394.
- Yurimoto, H., Nagasawa, H., Mori, Y., Matsubaya, O., 1994. Micro-distribution of oxygen isotopes in a refractory inclusion from the Allende meteorite. *Earth Planet. Sci. Lett.* 128, 47–53.
- Yurimoto, H., Ito, M., Nagasawa, H., 1998. Oxygen isotope exchange between refractory inclusion in Allende and solar nebula gas. *Science* 282, 1874–1877.